ELECTRON CLOUD EFFECTS – OBSERVATIONS, MITIGATION MEASURES, AND CHALLENGES IN RHIC AND SNS *

J. Wei†, M. Blaskiewicz, W. Fischer, H.C. Hseuh, U. Iriso, T. Roser, L. Wang, S.Y. Zhang
Brookhaven National Laboratory, New York, USA

Abstract

Electron cloud is one of the leading mechanisms that limit the performance of high intensity circular accelerators and colliders. In the Relativistic Heavy Ion Collider, multi-bunch electron cloud effects are observed both in the warm region and super-conducting region when the number of ion bunches and their intensities are raised beyond the design values. Vacuum-pressure rises, transverse tune shifts, and electron detector signals are observed at injection, upon transition crossing, and at top energy. Transverse emittance growth, fast instabilities, and beam loss also occur upon transition crossing. With the Spallation Neutron Source Ring, single-bunch electron cloud effects are expected for the high intensity proton beam. A comprehensive list of mitigation measures are implemented both to reduce the production of electron cloud and to control the beam stability. This paper intends to provide an overview of observations, performance limitations, and beam dynamics challenges pertaining to electron cloud build-up in high intensity, circular hadron accelerators.

1 INTRODUCTION

Since the first reports four decades ago, electron cloud has attracted the attention of accelerator physicists around the world [1]-[5]. During the recent years, electron-cloud effects are found to limit the performance of several high-intensity and high-brightness circular accelerators [6]. A fast, transverse electron-proton instability and the induced beam loss limits the beam intensity in the Proton Storage Ring (PSR) at the Los Alamos National Laboratory (LANL) [7]. Transverse emittance blow-ups caused by the electron cloud limit the luminosity in the lepton factories (BEPC, KEKB, PEP-II) [8]-[11]. During recent operations of the Relativistic Heavy Ion Collider (RHIC), vacuum-pressure rises associated with electron-induced gas desorption are found to limit the number of stored bunches and the beam intensity during high-intensity operations (Fig. 1) [12]-[14]. Electron-cloud phenomena include transverse tune shifts (KEKB, AGS Booster, RHIC), coupled-bunch (B factories, BEPC, PS, SPS) and single-bunch (KEKB, SPS, PSR, RHIC) instabilities, vacuum-pressure rise (RHIC etc.), emittance growth (KEKB, PEP-II, SPS, RHIC), beam diagnostics interference (RHIC, PS, SPS, PSR), and heat load on superconducting cryogenic wall (SPS beam experiments) [15].

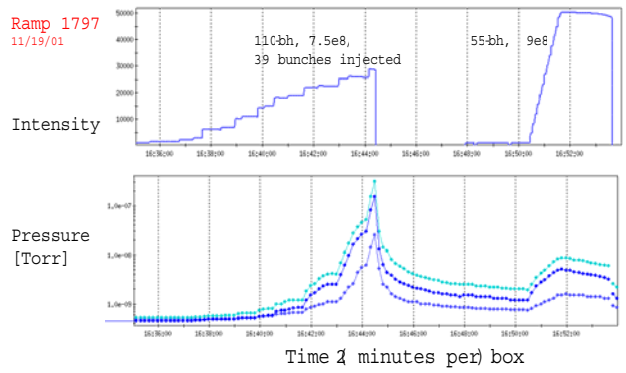

Figure 1: Vacuum-pressure rise in RHIC during gold-beam injection in year 2001 operation. The top curve indicates the total beam intensity as a function of time, and the bottom curves indicate the corresponding vacuum pressure at one location (BO11) of the ring. The horizontal scale is 2 minutes per box. The right-hand side shows the nominal operation when 55 bunches at 216 ns spacing, each containing 9×10^8 gold ions, are injected into the ring. The left-hand side shows that when the bunch spacing is reduced by half to 108 ns, the vacuum pressure increases dramatically even when only 39 bunches, each containing 7.5×10^8 gold ions, are injected.

Electron cloud is expected to be one of the performance-limiting mechanisms for the Spallation Neutron Source (SNS) accumulator ring currently under construction at the Oak Ridge National Laboratory [16]. When the full beam intensity of 2×10^{14} protons per pulse is accumulated in the ring, trailing-edge electron multipacting is expected to occur. Several mitigation strategies are adopted in the design, both in suppressing electron-cloud formation and in enhancing Landau damping.

This paper mainly discusses electron-cloud effects in RHIC and SNS. Section 2 briefly reviews key mechanisms of electron-cloud formation. Section 3 summarizes the experimental observations in the RHIC collider. Section 4 discusses theoretical expectations in the SNS accumulator ring. Mitigation measures adopted in RHIC and SNS are presented in Section 5. Beam-dynamics challenges are given in Section 6.

* Work performed under the auspices of the U.S. Department of Energy.
† jwei@bnl.gov

2 MECHANISMS

Key mechanisms pertaining to the formation of electron cloud are beam-driven electron multipacting and electron trapping. Depending on the beam parameters, the multipacting can be classified into several regimes: multiple short-bunch multipacting [4, 17, 18, 19], single long-bunch, trailing-edge multipacting [7, 20], and the intermediate regime. For the long-bunch and dc-beam [2, 3] cases, beam-induced trapping is critical to sustain electron concentration. For the short-bunch cases, trapping due to magnetic field is suspected to be responsible for the long electron lifetime over beam gaps [21].

2.1 *Multiple, short-bunch regime*

The phenomena of beam-driven multiple short-bunch multipacting have been observed in many lepton accelerators. The multibunch multipacting occurs if the transit time of the electrons crossing the vacuum pipe is comparable to the time between successive bunches, and if the electrons gain enough energy to produce more than one secondary electron when they hit the vacuum-pipe wall [4].

The multiple, short-bunch regime is defined as

$$\zeta_m \equiv \frac{2b}{s_b}\frac{\beta}{\beta_e} \geq 1 \tag{1}$$

where the short-bunch multipacting parameter ζ_m is defined as the ratio between the transit time of the characteristic electron crossing the vacuum pipe to the time between successive bunches, s_b is the distance between the subsequent bunches, b is the average radius of vacuum pipe, βc is the velocity of the beam, and $\beta_e c$ is the characteristic velocity of the electrons [4, 22]. In the case that $\zeta_m \approx 1$, the energy gained by the electron from the passage of the beam bunch is approximately given by

$$\Delta E_e = m_e c^2 \left[\sqrt{\left(\frac{2r_e N_0}{\beta b}\right)^2 + 1} - 1\right] \approx 2m_e c^2 \left(\frac{r_e N_0}{\beta b}\right)^2 \tag{2}$$

where $r_e = e^2/4\pi\epsilon_0 m_e c^2$ is the classical radius of electron, N_0 is the number of particle in the beam bunch, the second relation is true if the electron motion is non-relativistic, and

$$\zeta_m \approx \frac{\beta^2 b^2}{r_e N_0 s_b}. \tag{3}$$

In the general case that $\zeta_m > 1$, the energy gain needs to be analyzed numerically [23]. In order to sustain a multipacting, the energy gained by the electron upon one or more beam bunch passage must be such that the overall electron-induced secondary-emission yield Y_{ee} (SEY) satisfies

$$Y_{ee} > 1. \tag{4}$$

Multibunch electron multipacting may occur for almost any value of ζ_m satisfying Eq. 4 [8].

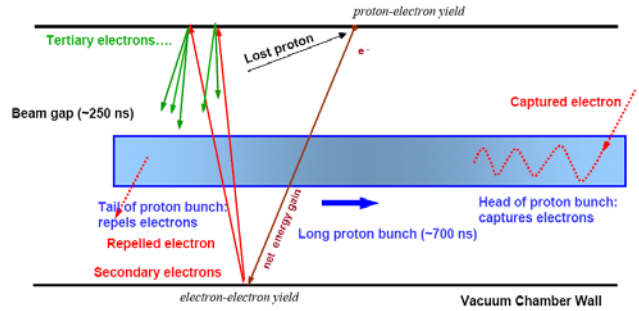

Figure 2: Beam-induced electron multipacting at the trailing edge of a long proton-bunch. The transit time of the electrons across the beam pipe is much shorter than the passage time of the proton bunch.

The occurrence of electron-cloud multipacting build-up depends strongly on the beam intensity and the secondary-emission yield of the beam-pipe surfaces. The multiple short-bunch multipacting is sensitive to the bunch spacing and bunch pattern, and insensitive to the bunch length and profiles when the condition of Eq. 1 is satisfied. The effect is usually stronger for regions of smaller vacuum-pipe aperture where the beam field at the wall and the electron crossing frequency are both high. Both multi-bunch and single-bunch head-tail instabilities are observed. Mechanisms that sustain electron concentration include trapping by the magnetic fields (e.g., quadrupole-field trapping resonant to the bunch passage [21]) and near-elastic reflection of low-energy electrons [24].

2.2 *Single, long-bunch regime*

The phenomena of beam-driven single, long-bunch multipacting are observed in routine operations in the PSR and expected in the SNS ring. Single-bunch, trailing-edge multipacting starts to dominate if the bunch length is long enough to sustain multiple passes of electrons. As shown in Fig. 2, electrons are attracted by the rising beam particle density as the beam potential increases [25, 26]. The motion is characterized by the electron bounce-frequency

$$\omega_e = c\sqrt{2\pi r_e n_p} \tag{5}$$

where n_p is the volume density of the beam. After the passage of the beam density peak, electrons are released and accelerated by the part of the beam of decreasing density (trailing edge of the beam density distribution). The number of electrons grows dramatically upon such trailing-edge multipacting, as observed at the PSR [7].

The single, long-bunch regime is defined as

$$\zeta_s \equiv \frac{4b}{s_b B_f}\frac{\beta}{\beta_e} \ll 1 \tag{6}$$

where the long-bunch multipacting parameter ζ_s is defined as the ratio between the transit time of the characteristic electron crossing the vacuum pipe to the passage time of

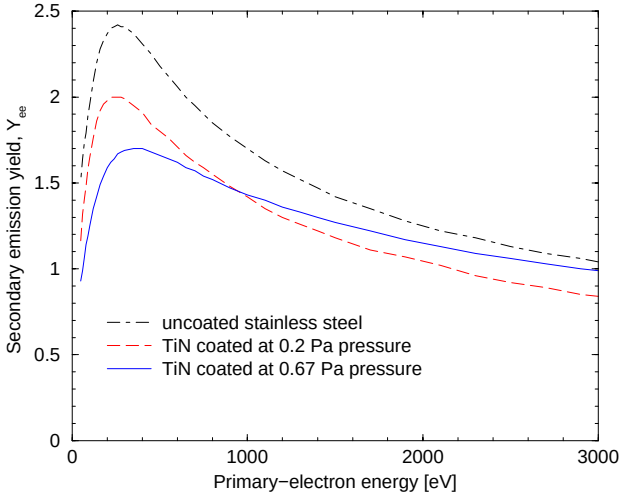

Figure 3: Secondary-electron yield for various coating conditions of the SNS ring chamber measured at CERN. Magnetron (dc) sputtering is used to coat the surfaces with 0.1 μm TiN. Surfaces coated at a pressure of 0.67 Pa, which has a lower peak Y_{ee} but a higher outgassing-rate comparing with those coated at a pressure of 0.2 Pa, are adopted [27].

half of the beam bunch, and B_f is the bunching factor [22]. When the electron motion is non-relativistic, the energy gained by an electron is approximately given by

$$\Delta E_e \approx 4 m_e c^2 \beta b \sqrt{\frac{r_e N_0}{s_b^3 B_f^3}} \tag{7}$$

while

$$\zeta_s \approx \frac{\beta b}{\sqrt{r_e N_0 s_b B_f}}. \tag{8}$$

Single-bunch multipacting occurs if the energy gained by the electron is such that

$$Y_{ee} > 1. \tag{9}$$

Fig. 3 shows examples of the measured secondary yields as functions of the primary electron energy on vacuum-chamber surfaces of the SNS ring.

Electron-cloud build-up due to the single-bunch multipacting is typically not sensitive to the bunch spacing, while electron survival between the bunch passage is sensitive to the trapping in the beam gap. The build-up depends critically on the length of the beam bunch and the variations in its longitudinal density, which determine the energy gain and the multipacting duration. The effect can be stronger for regions of larger vacuum-pipe aperture where higher energy gained over a longer path-length results in a higher secondary yield, although the longer path-length may also reduce the multipacting frequency. Upon acceleration by the beam, the electron energy is typically below kV level. Associated with the electron-cloud build-up, single-bunch, fast transverse instabilities are observed [7]. Main trapping mechanisms include attraction of the electrons due to

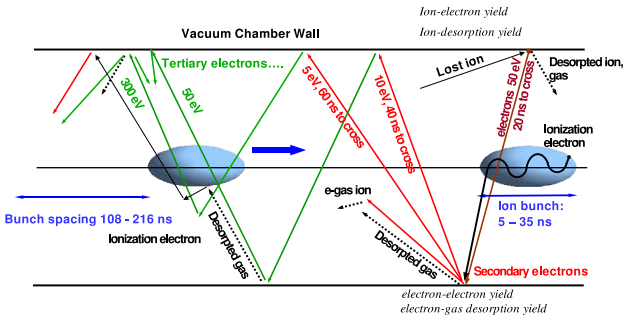

Figure 4: Electron build-up at BNL's RHIC as an example of intermediate-regime beam-induced electron multipacting. The time between successive bunches is typically 108 ns when the multipacting occurs. The energy gain due to bunch passage is from about 50 to 300 eV.

the increasing beam density at the rising density edge of the bunch, reflections from the vacuum-chamber wall, and trapping by the beam residual in the gap. Trapping by the magnetic fields (e.g., quadrupole field) is typically weak due to lack of resonance mechanism [25]).

A coasting, dc beam is a special case of the long-bunch regime. In this case, the electrons are trapped by the constant beam potential, and the electron density may accumulatively increase leading to vacuum pressure rise and two-stream instabilities when the thresholds are exceeded [2, 3].

2.3 *Intermediate regime*

RHIC belongs to the intermediate regime where the transit time of the electrons crossing the vacuum pipe is comparable to the bunch length, as shown in Fig. 4. Between the subsequent bunches, the electrons typically reflect from the vacuum chamber wall for several times.

Upon acceleration by the beam bunch, the electrons gain energy up to several hundred eV, and hit the wall with an average SEY $Y_{ee,0}$ typically much larger than 1. Upon subsequent impacts on the wall, the electron energy is low (typically below 10 eV) due to lack of beam potential, and the average secondary-emission yield $Y_{ee,i}$ ($i = 1, \ldots$) is smaller than 1. We define the characteristic SEY $Y_{ee,C}$ as the product of the average SEY of N_{ee} reflections between two subsequent bunch passage. The threshold for the multipacting in this regime corresponds to the condition when

$$Y_{ee,C} \equiv \Pi_{i=0,1,\ldots,N_{ee}} Y_{ee,i} > 1 \tag{10}$$

where

$$Y_{ee,0} > 1, \text{ and } Y_{ee,i} < 1 \text{ for } i = 1, \ldots, N_{ee} \tag{11}$$

Multipacting in the intermediate regime shares the features of both the short-bunch and long-bunch regimes. The build-up is not only sensitive to the bunch spacing and bunch pattern, but also sensitive to the bunch length and peak intensity. With a shorter bunch spacing, the number of low-energy electron passages N_{ee} is reduced, increasing

the chance of exceeding multipacting threshold $Y_{ee,C} > 1$. With a shorter bunch length and higher peak beam intensity, the electron energy gain upon bunch acceleration becomes higher, leading to a higher secondary emission yield $Y_{ee,0}$ and $Y_{ee,C}$. Mechanisms that sustain electron concentration include reflections from the vacuum-chamber wall, trapping by the beam residual in the gap, trapping by the magnetic fields, and possible secondary ionization and trapping [28].

In the following section, we present observations pertaining to electron cloud formation in RHIC.

3 RHIC OBSERVATIONS

The RHIC collider is comprised of two quasi-circular rings (blue ring and yellow ring) each consisting of superconducting magnets contained in 4 K cryostats (Table 1). Counter-circulating ions of various species from proton to gold can be stored in each ring to intersect with each other at up to six room-temperature locations.

Table 1: Typical machine and beam parameters pertaining to electron cloud in RHIC.

Ring circumference	3833.8	m
Aperture, IR (2/6/8/10, 4/12)	7, 12	cm
Aperture (arc, triplet)	7, 13	cm
Beam species	p - Au	
Energy, injection - top, Au	9.8 - 100	GeV/u
Energy, injection - top, p	24.3 - 100	GeV
Transition energy, γ_T	22.9	
Rebucketing energy, $\gamma_{\rm top}$	107.5	
Bunch intensity, p, Au	10^{11}, 10^9	
Bunch spacing	108, 216	ns
Bunch length, full	35 - 5	ns
Electron bounce frequency	150 - 400	MHz
Peak bunch potential	0.25 - 1.6	kV
e^- energy gain upon acceleration	50 - 300	V

During normal operations, ion bunches at 216 ns spacing, each containing up to 10^{11} charges (e.g., 10^9 $^{197}Au^{79+}$ or 10^{11} protons), are injected into each ring and accelerated to the top energy for hours of storage. During the acceleration cycle, the bunch length reaches the minimum, and the peak intensity reaches the maximum when the beam crosses the transition energy ($\gamma_T \approx 22.9$), and when the beam is transferred from the acceleration RF system (28 MHz) to the storage RF system (200 MHz) at the beginning of the storage (rebucketing, $\gamma_{\rm top} \approx 107.5$).

Sources of seed electrons in RHIC are expected to be gas ionization and beam-loss induced surface emission and desorption. The electron cloud becomes measurable only if the threshold for intermediate-regime multipacting and trapping, as discussed in the previous section, is exceeded. Observables include vacuum pressure rise in the warm-bore region, gas density increase in the cold-bore region, electron flux on the wall, as well as bunch-dependent coherent tune shifts, transverse instabilities, transverse emittance growths, and beam losses.

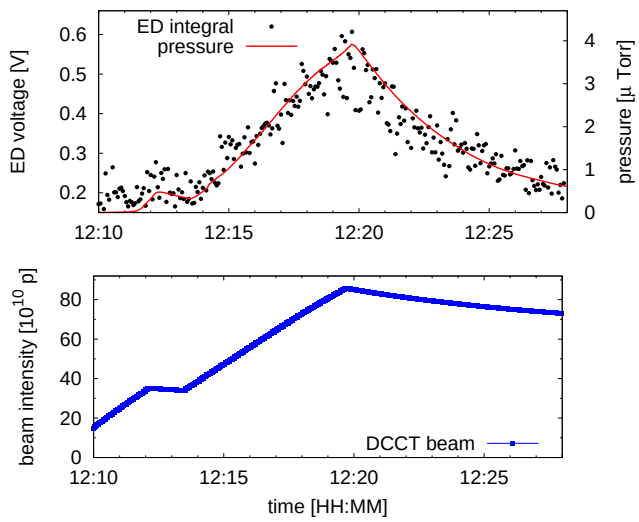

Figure 5: Beam intensity, vacuum pressure, and integral electron flux as functions of time during the injection of beams of about 0.78×10^{11} protons per bunch with 108 ns bunch spacing.

3.1 *Vacuum pressure rise and electron flux*

One of the most pronounced phenomena in RHIC pertaining to electron cloud is the vacuum pressure rise when the spacing between full-intensity bunches is reduced, as shown in Fig. 1 [12]. Pressure rise often occurs during beam injection when a large number of bunches are injected with a reduced bunch spacing (108 ns in comparison to the design value of 216 ns), and upon transition crossing and rebucketing when the bunch peak intensity reaches the maximum. Figs. 5 and 6 show a direct correlation between the vacuum pressure and the integral electron flux on the wall measured by a retarding-field electron detector [14].

The pressure rise often occurs in the interaction region (IR) where beams in the two rings are both present effectively doubling the local beam intensity, in regions where unbaked surfaces are exposed to the beam, and in regions where high SEY material surfaces (e.g. Be vacuum chamber in the PHOBOS experimental region) are present. Fig. 7 shows an example of the electron flux on the IR vacuum-chamber wall measured by the electron detector, where even the intensity threshold for electron multipacting is not exceeded in each individual ring, the multipacting occurs in the interaction region. Fig. 8 shows that although a beam gap of 432 ns appears to suppress the electron multipacting, the suppression is incomplete since the multipacting re-occurs in a much shorter time [14].

In addition to the beam-induced electron multipacting, beam-induced vacuum run-away caused by gas desorption from the pipe surface and subsequent ionization by the beam may also contribute to a pressure increase. During

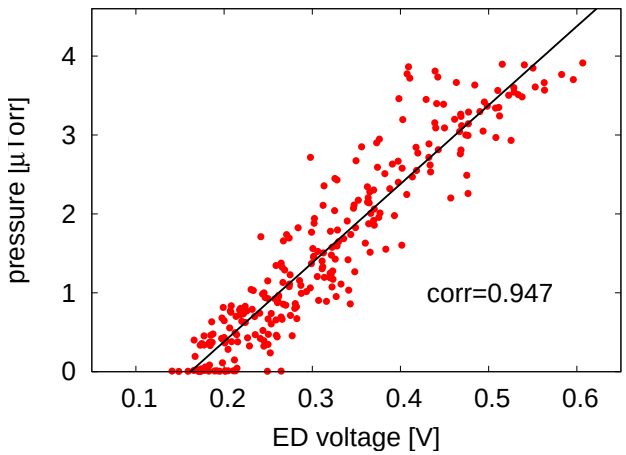

Figure 6: Vacuum pressure as a function of the measured integral electron flux (i.e. electron detector voltage) on the wall corresponding to Fig. 5.

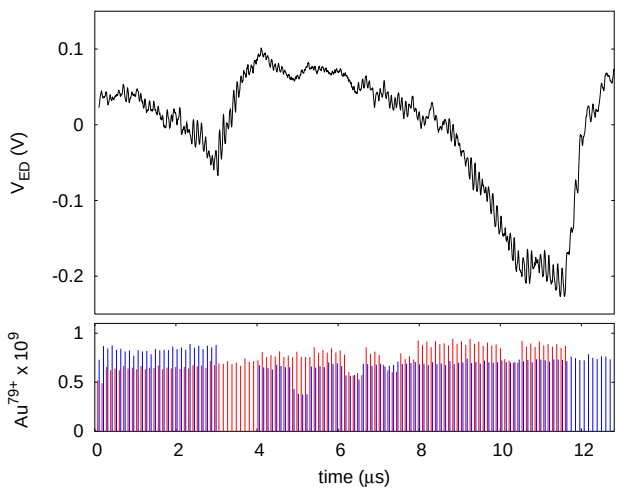

Figure 7: Electron flux measured at injection in the RHIC IR where two gold beams of 108 ns bunch spacing share the common beam pipe. The two colors in the bottom figure indicate the bunch pattern in the two rings. An ac-coupled amplifier is used with a low-frequency cut-off of about 300 kHz (The integral over one revolution period of 12.8 μs is zero). The grid is not biased. The collector is biased at 50 – 100 V positive.

the year 2003 - 2004 operations, pressure rises in the un-baked regions (un-baked stochastic cooling kickers and un-baked collimator jaws) are attributed to the increase in both the electron secondary-emission yield and the gas desorption yield in comparison with that of the baked surfaces [29].

3.2 *Tune shifts and electron-ion instability*

During the RHIC acceleration cycle, instability is likely to occur upon transition crossing due to lack of synchrotron oscillation and synchrotron frequency spread [30]. Transition-energy jump is used to effectively increase the transition crossing rate. However, transverse instabilities of both slow (∼100 ms) and fast (∼15 ms) growth rates are still observed [31]. Some cases of transition instability are not correlated to the observation of electron cloud, and are often cured by the adjustment of the timing and magnitude of the chromaticity jump, and the activation of octupole magnets at transition [32].

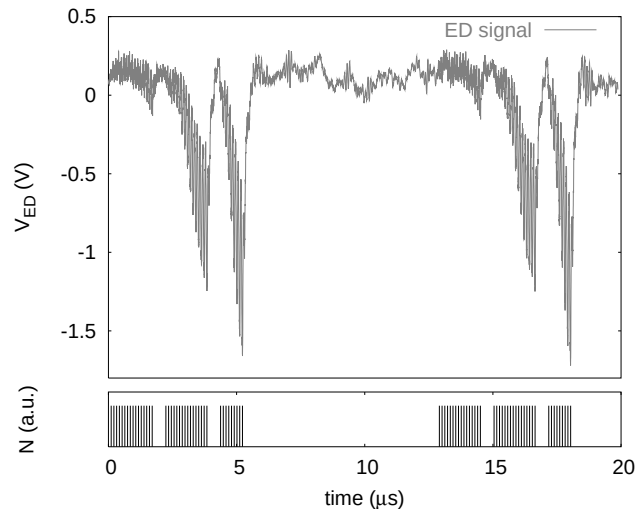

Figure 8: Electron flux measured at injection at 108 ns bunch spacing with a fill pattern of 16-bunch beam, 4-bunch gap, 16-bunch beam, 4-bunch gap, then 9-bunch beam, and 71-bunch gap. The signal is again ac-coupled and averages to zero over one revolution of 12.8 μs.

Systematic studies on a fast instability at transition are in progress during year 2004 - 2005, indicating correlation to the electron cloud [33]. Fig. 9 shows the transverse coherence signal defined as the time-averaged rms amplitude of the transverse centroid displacement. A transverse instability occurs immediately after transition for about 0.1 s, leading to beam loss and emittance growth that are increasingly severe for later bunches of the bunch train, as discussed in the next section. This fast instability and beam loss also results in bunch-dependent longitudinal distributions, as shown in Fig. 10.

Bunch-dependent coherent tune shifts in both the horizontal and vertical directions have been observed during the injection of proton bunches at an intensity of 0.3×10^{11} per bunch and 108 ns bunch spacing. The tune shift of about 2.5×10^{-3} corresponds to an electron density of up to 2 nC/m [13]. Measurement of bunch-dependent tune shift during acceleration ramping is yet to be attempted.

3.3 *Emittance growth and beam loss*

Beam experiments during year 2004 - 2005 indicate that with the beam in a single (blue) ring at 108 ns bunch spacing of 5×10^9 copper ions per bunch, electron cloud ef-

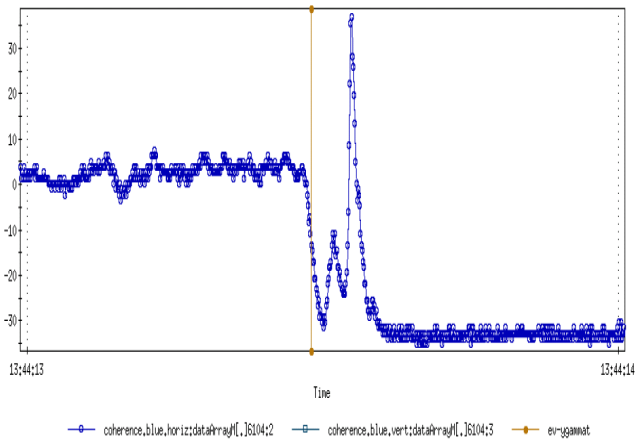

Figure 9: Horizontal coherence observed on bunch #39 indicating instability after transition. 40 bunches, each of 5×10^9 copper ions, are accelerated at 108 ns spacing. The shift in baseline is due to the orbit change upon transition jump. The coherence that corresponds to an electron-ion instability causing a large beam loss, occurs within about 0.1 s immediately after transition crossing [33].

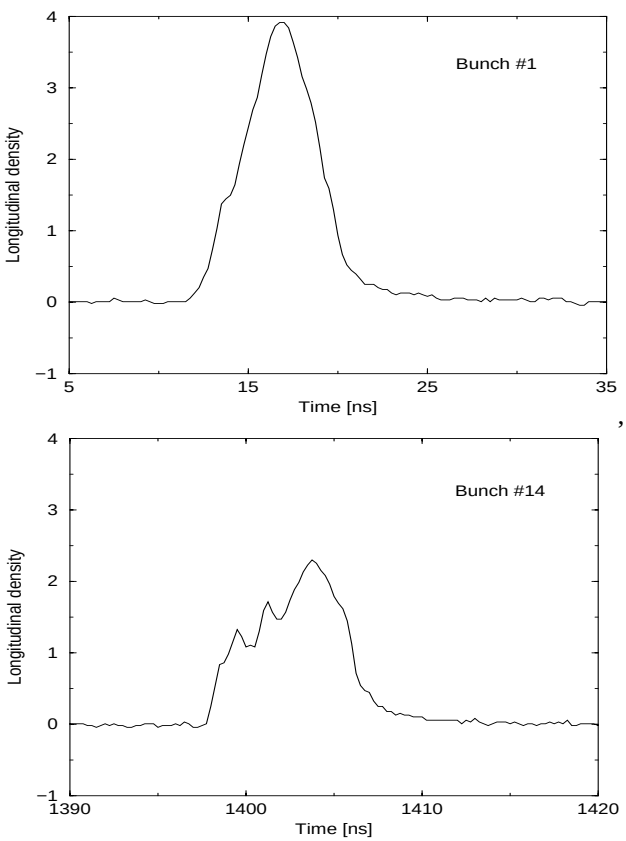

Figure 10: Longitudinal profiles of the first (top) and the 14th (bottom) bunch immediately after transition in the RHIC blue ring. The beam parameter is the same as Fig. 11 [33].

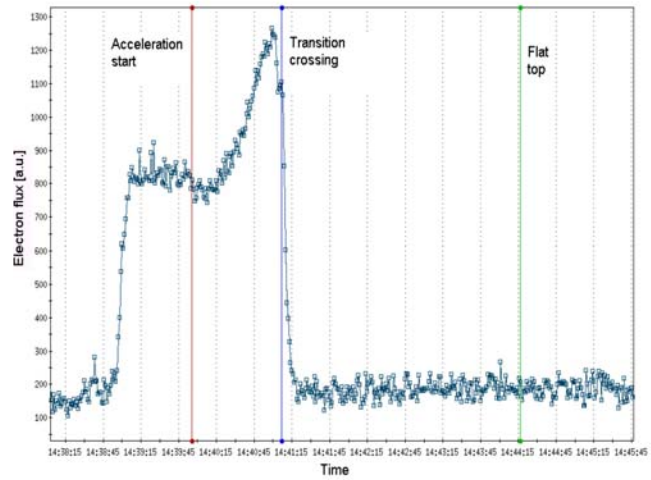

Figure 11: Measured peak electron flux on the wall as a function of time during the RHIC operation cycle. 40 bunches, each of 5×10^9 copper ions, are accelerated at 108 ns spacing. The flux increases as the beam approaches the transition energy, and disappears due to the large beam loss at transition [33].

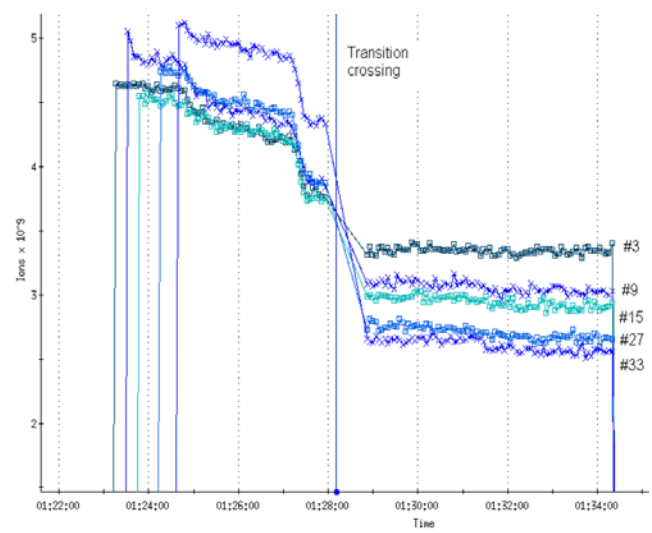

Figure 12: Measured bunch-dependent intensity reduction near transition crossing in RHIC. The beam parameter is the same as Fig. 11. The wall-current monitor data is not logged for about 1 minute near transition [33].

fects dominate the acceleration ramp [33]. As the beam approaches transition, the vacuum pressure and the electron flux (Fig. 11) both increase due to the increase of the peak beam intensity. On the other hand, the electron cloud impacts the beam mostly at the time of transition crossing (within about 0.1 s) when the beam particle motion is non-adiabatic, causing electron-ion instability (Fig. 9 obtained from the beam-position monitor data), beam loss (Figs. 12 and 13 obtained from the wall-current monitor data), and emittance growth (Fig. 14 obtained from the ionization pro-

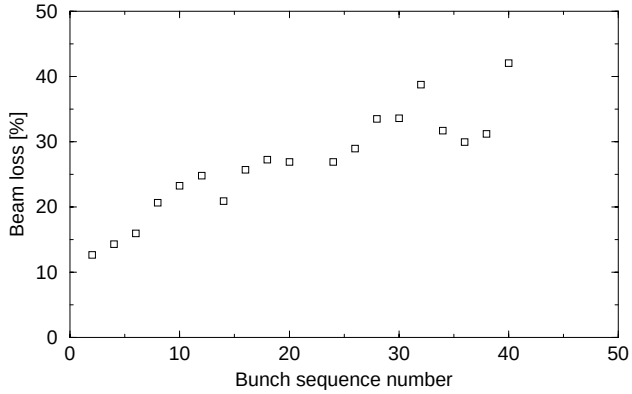

Figure 13: Beam loss at transition as a function of bunch sequence number in the 40-bunch train of copper ions in the RHIC blue ring. The beam parameter is the same as Fig. 11 [33].

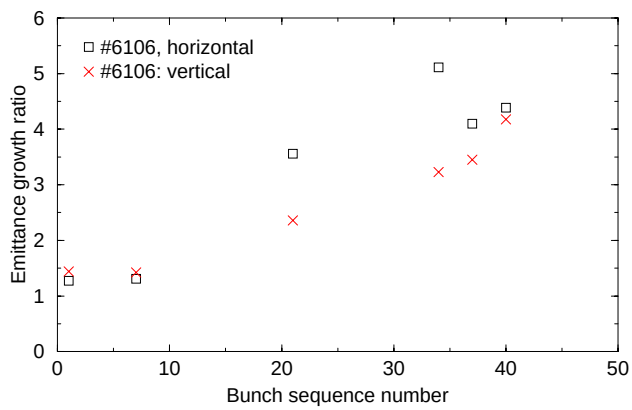

Figure 14: Beam horizontal emittance growth at transition as a function of bunch sequence number in the 40-bunch train in the RHIC blue ring. The beam parameter is the same as Fig. 11 [33].

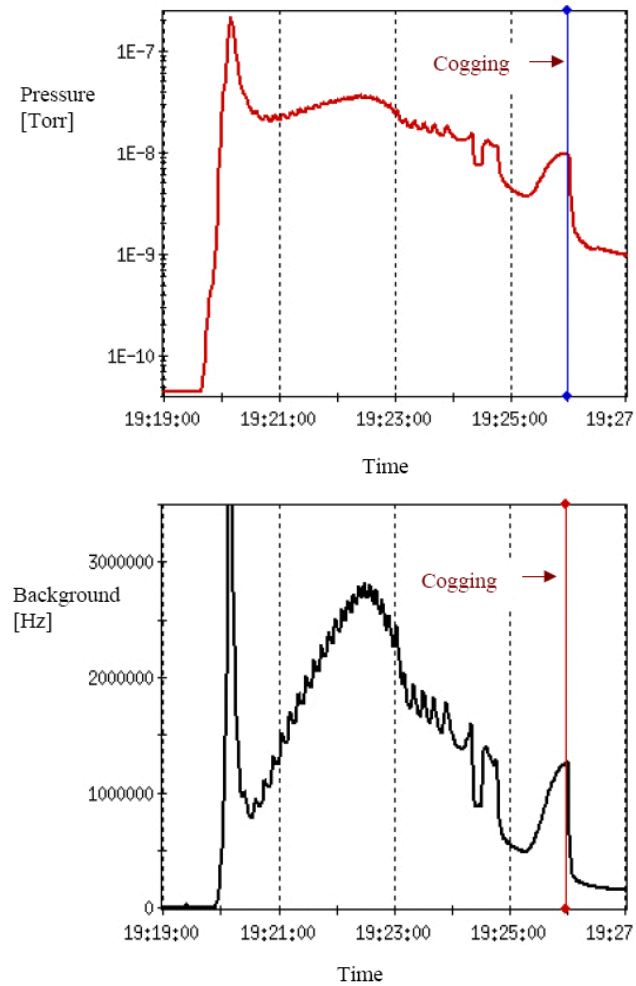

Figure 15: Transition pressure rise at high beam intensity causes high experimental background in the d-Au operation in RHIC. After beam-collision starts, the pressure reduces; but the corresponding background is still 200 kHz, much higher than the coincidence rate of 7 kHz.

file monitor data).

Systematic studies indicate that families of octupole magnets can enhance Laudau damping and effectively reduce the electron-ion instability beam loss. A lower RF voltage at transition also reduces the peak intensity and the momentum spread, effectively reducing both the chromatic [30] and the electron-cloud effects [33] at transition.

3.4 *Background and interferences*

Occasional, excessive experimental background in the interaction region is attributed to the ionization when the vacuum pressure rises due to electron cloud (Fig. 15), and to secondary shower from direct beam loss on the wall [34].

Electron cloud is also found to interfere with the beam diagnostics in RHIC. The RHIC ionization profile monitor (IPM) system is based on collecting electrons produced from controlled gas ionization with the circulating beam. Sweeping electrodes are used, and the multi-channel plates for electron collection need to be recessed from the vacuum-chamber wall to avoid superfluous signals (Fig. 16) [35].

3.5 *Cold-region density increase*

The molecular density in the 4.5 K temperature cold-bore region of the superconducting magnets has been indirectly measured with cold-cathode gauges connected through 1.5 m long, 2.5 cm diameter conduits with about 1 l/s conductance, capable of measuring the effective pressure at 10^{-10} Torr level [29]. As shown in Figs. 17 and 18, the molecular density increases in the cold and warm regions are similar in time scale and magnitude. An increase of up to three orders of magnitude in the effective pressure is observed both in the triplet region (Q1-Q2-Q3) and in the arc region (Q9-Q20-Q9) around the machine (Fig. 19). Temperature rise is not observed at a resolution of about 0.01 K

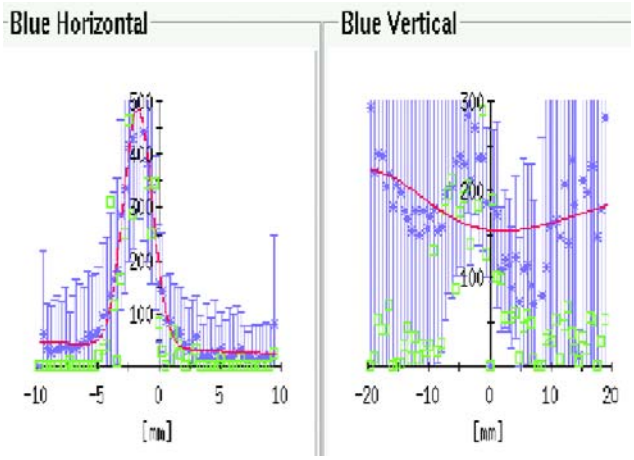

Figure 16: Comparison of beam profiles measured by the RHIC IPM in the horizontal plane where the multi-channel collecting plates are recessed from the wall, and in the vertical plane where they are not (courtesy R. Connolly).

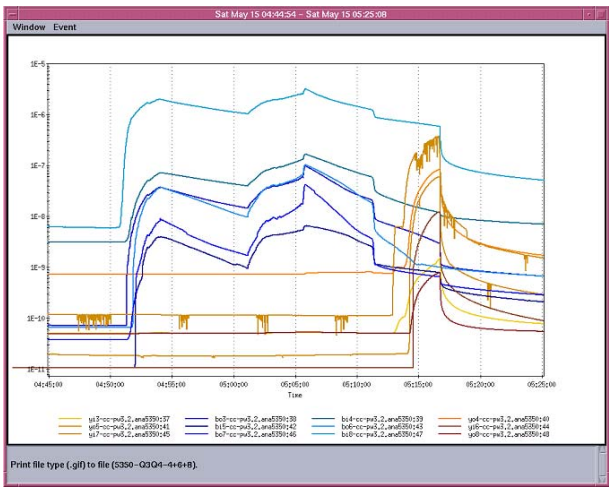

Figure 17: Effective vacuum-pressure rise that corresponds to the molecular density increase in the region between superconducting quadrupole magnets Q3 and Q4 at 4.5 K temperature in RHIC. The data is logged every 5 minutes.

corresponding to a heat load of about 5 W per 100 m.

The effective pressure rise in the cold region is attributed to lack of active pumping during most machine shutdowns. An estimated 10 to 100 mono-layers of molecules are accumulated. Direct measurement of the electron flux in the cold region has not been possible, especially since all the beam-position monitors are grounded.

4 SNS EXPECTATIONS

The Spallation Neutron Source (SNS) accumulator ring is designed to accumulate, via H^- injection, protons of 2 MW beam power at 1 GeV kinetic energy at a repetition rate of 60 Hz. At such beam intensity, electron-cloud is expected to be one of the intensity-limiting mechanisms that complicate ring operations (Table 2).

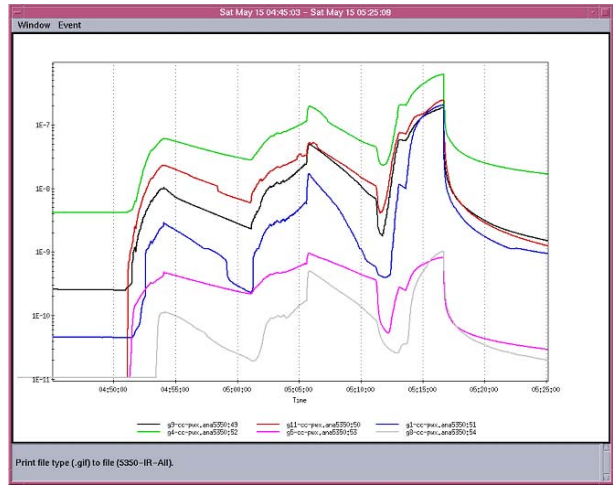

Figure 18: Corresponding to Fig. 17, the vacuum-pressure rise in the IR region at the room temperature.

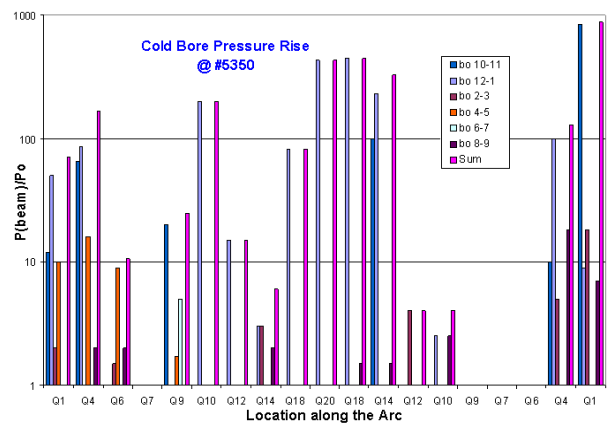

Figure 19: Ratio of the effective vacuum pressure between the beam-induced and the static conditions in RHIC.

Sources of seed electrons in SNS are mainly expected to be the stripped electrons from the stripping foil in the injection region, emission from the scraper and collimator surfaces as lost protons are collimated, and from residual-gas ionization especially when vacuum pressure rises. The electron density can be greatly enhanced by the beam-induced multipacting at the trailing edge of the bunch, as shown in Fig. 20 [25]. Serious electron cloud effects may occur if the stripped electrons are not properly collected, if an excessive amount of beam is lost at the collimators, if the surface SEY deteriorates, and if the amount of beam residual in the beam gap is excessive.

4.1 Injection stripped electrons

During the H^- charge-exchange injection at 1 GeV beam energy, the stripped electrons of 545 keV kinetic energy and 2 kW power are collected by a water-cooled catcher

Table 2: Typical machine and beam parameters pertaining to electron cloud in the SNS accumulator ring.

Ring circumference	248.0	m
Aperture (arc, straight)	21, 30	cm
Beam species	proton	
Kinetic energy	1	GeV
Bunch intensity	2×10^{14}	
Beam gap length	250	ns
Bunch length, full	700	ns
Electron bounce frequency	$\sim$ 175	MHz
Peak bunch potential	5 - 10	kV
e^- energy gain upon acceleration	0 - 300	V

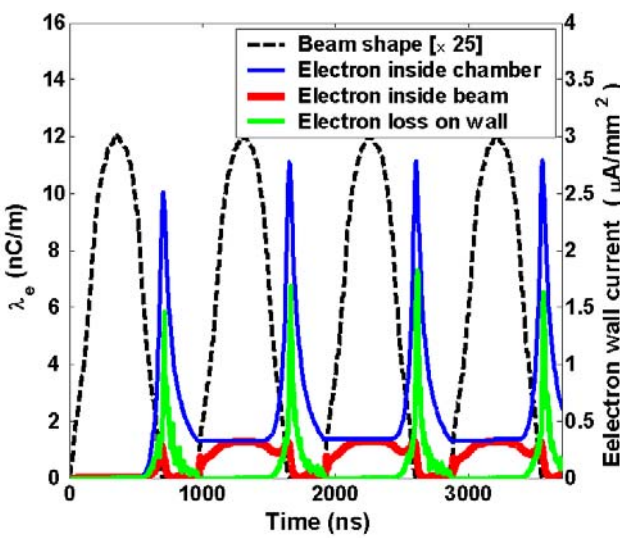

Figure 20: Computer simulation of the beam-induced electron multipacting in the non-magnetic region of the SNS ring. The beam intensity is 2×10^{14} per bunch. The peak SEY is assumed to be 1.8. The peak neutralization level is about 1.5% within the rms beam radius, and about 10% on average within the beam pipe.

(Figs. 21, 22). These electrons back-scatter from the catcher and the vacuum chamber, resulting in a high concentration of electrons with a broad energy spectrum. The injecting- and circulating-beams impacting on the foil produce secondary emission of electrons at tens of eV energy. The injecting- and circulating-beam also produce knock-on electrons at a high energy (up to several MeV). The stripping-foil, operating at a high temperature around 2000 K, emits thermionic electrons at low energy [36].

An accurate control of electron collection is essential in minimizing the electron cloud in the injection region. As shown in Fig. 23, the catcher consists of multiple tapered blades of low charge-state (carbon-carbon) to reduce back-scattering [38]. Video cameras are used to monitor both the stripping foil and the electron catcher (Fig. 24).

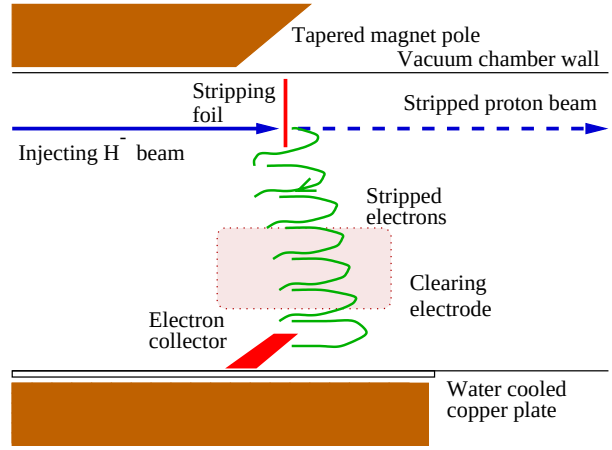

Figure 21: Collection of stripped electrons during the injection of H^- beam at the SNS ring. The stripped electrons are guided by a magnetic field and collected by a water-cooled device of heat-resistant material [37].

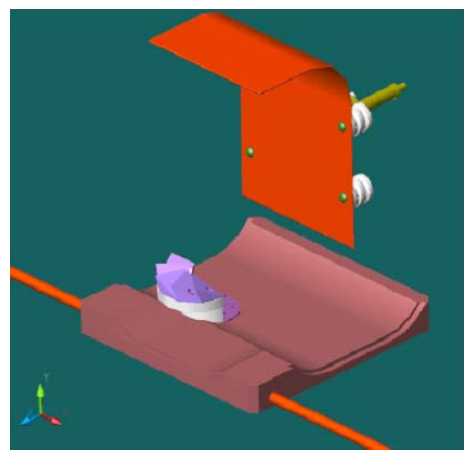

Figure 22: Devices to control electron cloud in the injection region of the SNS ring. The half-disk C-C catcher is attached to the water-cooled copper plate at the bottom of the vacuum pipe. The clearing electrode can supply 10 kV voltage [37].

4.2 *Collimation region electrons*

Protons incident on the collimator surfaces produce secondary electrons. Depending on the energy of the beam and the incident angle, the secondary electron-to-proton yield can greatly exceed 1 when the incident beam is nearly parallel to the surface [39], as shown in Fig. 25. Although a serrated surface reduces the generation of secondary-emission electrons, it is practically ineffective since protons incident on the front edge of the teeth easily escape from the collimator body due to the long proton stopping-length (about one meter) at 1 GeV energy. It is crucial to use a two-stage collimation system with a primary thin scraper (Fig. 26) to enhance the impact parameter to the secondary collimator (Fig. 27).

The SNS ring collimation system is designed to collect

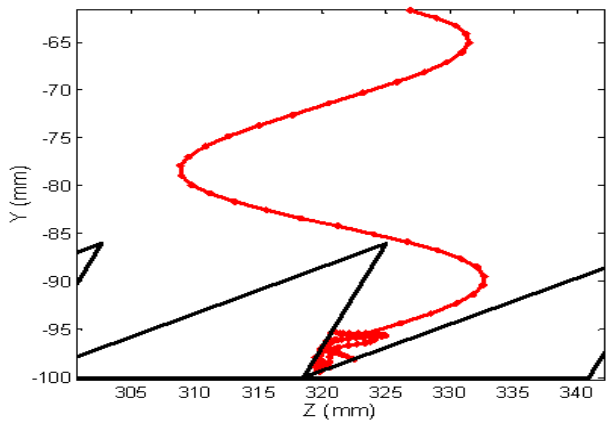

Figure 23: Trajectory of the incident and back-scattered electron from the SNS injection electron catcher [38].

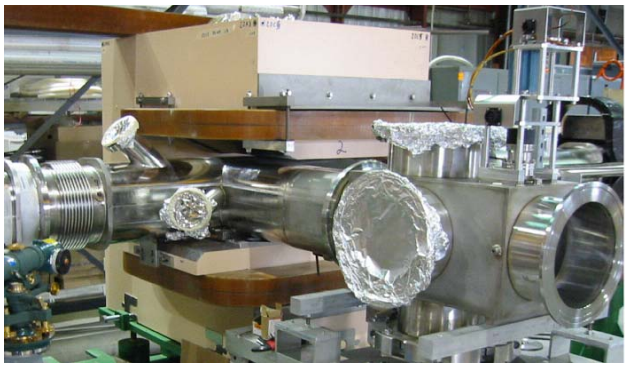

Figure 24: SNS injection foil chamber and nearby devices showing video ports to monitor the stripping foil and the electron catcher.

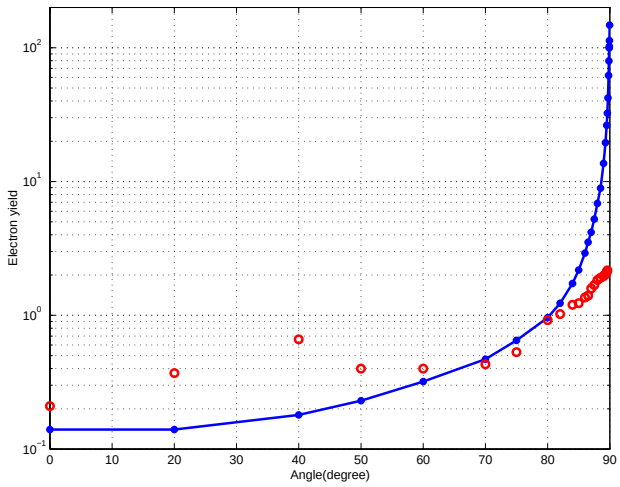

Figure 25: Proton-induced secondary-emission yields of electrons as functions of the incident angle for 28-MeV protons striking a flat (solid line) and a serrated (open circles) stainless-steel surface (courtesy P. Thieberger).

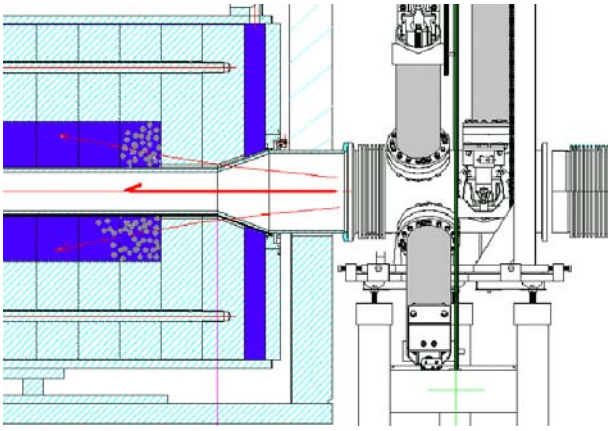

Figure 26: Schematics of the SNS ring primary scraper assembly and the down-stream shielding. The scraper assembly contains 4 thin tantalum blades transversely placed at 45° angle. The down-stream shielding has a similar structure as the ring collimators shown in Fig. 27 (courtesy H. Ludewig and N. Simos).

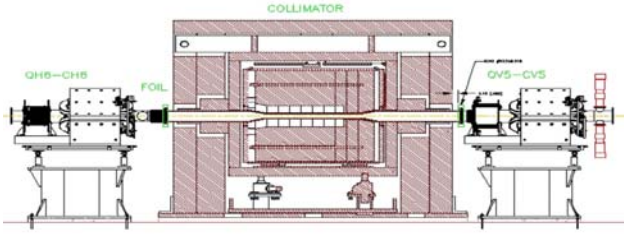

Figure 27: Schematics of the SNS ring collimator showing layers of material for radio-activation containment. The effective length is about 1.5 m. The collimator is designed to withstand an average beam power of up to 10 kW at 1 GeV kinetic energy (courtesy H. Ludewig, N. Simos, and G. Murdoch). The SNS ring has two such collimators, both located at optimized betatron phase advances down-stream of the primary scraper and its shielding [40].

more than 90% of the lost beam in the ring [40]. Comparing with other regions where the beam loss is typically below 1 W/m for hand-on maintenance, the collimation region expects a beam loss of about 500 W/m. In order to avoid frequent maintenance in such high radio-activated region, the secondary collimators are made non-adjustable (Fig. 27) without attaching any electron-cloud mitigation devices (like clearing electrodes and solenoids).

The small aperture of the collimators (Fig. 28) helps to reduce the trailing-edge electron multipacting in the most critical region where beam loss is expected to be the greatest. As shown in Fig. 29, the lower energy gain in the collimator region results in an effectively lower secondary yield. In areas of larger aperture between the collimators, which are more susceptible to the multipacting, solenoids are wound to suppress the electron cloud.

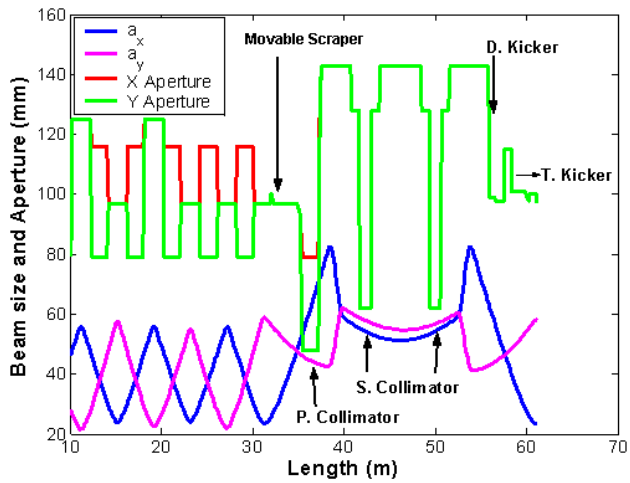

Figure 28: Beam acceptance envelope at 480 $\pi\mu$m in comparison with the physical aperture in the horizontal and vertical directions in the SNS collimation region [41].

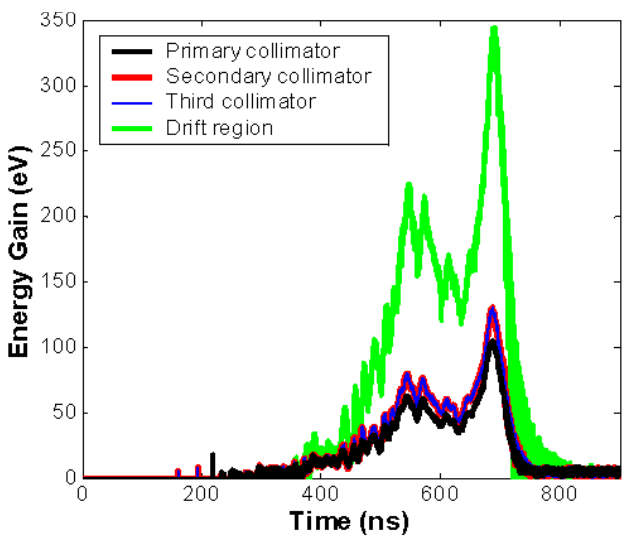

Figure 29: Electron energy gain upon beam passage in small-aperture (10 $\sim$ 14 cm) area of the SNS collimation region in comparison with the gain in a typical large-aperture drift region (28 cm) [25].

4.3 *Ionization*

The rate of electron line-density increase per unit length of circumference is given by the relation

$$\frac{d^2\lambda_e}{dtds} = \frac{\rho_m \beta I \sigma_{ion} P}{e} \tag{12}$$

where I is the beam current, σ_{ion} is the cross-section, P is in units of Torr. At the room temperature of 300 K, the molecular density ρ_m is about 3.3×10^{22} m^{-3}. For the SNS ring at a pressure of 10^{-8} Torr, a total number of 2.6×10^9 electrons per turn, or 1.7 pC/m of charge per turn, is produced when the proton intensity is 2×10^{14}. The ionization electrons, however, are likely to be trapped in the long proton bunch until the very end of the bunch passage, thus not participating in the trailing-edge multipacting process [25].

5 MITIGATION MEASURES

Control of the electron-cloud effects in both the RHIC and the SNS ring involves design and operational optimization to minimize the uncontrolled beam loss, enhancement of Landau damping, and suppression of electron generation.

Minimization of the uncontrolled beam loss is of primary importance for the SNS ring [6]. At the design stage, a large transverse acceptance and long, uninterrupted straight-sections are two important aspects considered on the lattice. The two-stage collimation system also plays an essential role in localizing the beam loss to controlled areas. For RHIC, intra-beam scattering causes routine beam loss during the beam storage. The collimation system can effectively control the vacuum pressure rise and reduce the experimental background.

Enhancement of Landau-damping helps to raise the instability threshold. For the SNS ring, a large vacuum-pipe aperture in the high-dispersion area and a large RF voltage provide sufficient momentum acceptance of $\pm1\%$ for a 480$\pi\mu$m transverse acceptance; longitudinal painting is used to expand the momentum spread of the injected beam; lattice sextupole families are used for chromatic adjustments, to either improve momentum acceptance or enhance damping; and, octupoles are also available for a possible future enhancement. For RHIC, octupole correction magnets are used to suppress the transverse instability near transition crossing.

Suppression of electron generation mainly includes measures to reduce the electron multipacting as discussed in the following.

5.1 *Surface treatment*

The inner surface of the stainless-steel pipe in the RHIC warm region are coated in subsequent sections with non-evaporative getter (NEG) to lower both the secondary emission and desorption yield, and to increase local vacuum pumping [29]. Beam experiments confirmed the effectiveness of the coating in reducing the vacuum pressure rise [42]. In year 2004, part of the RHIC cold region (four arc sections and four triplet sections) is pumped down to a vacuum pressure below 1×10^{-2} Torr before the cryogenic cool down to reduce the physi-sorbed gas to sub-monolayers.

The inner surface of the entire SNS ring is coated with TiN. Coated chambers are tested for conductivity and rise-time response. With a variation within 20%, the thickness of 0.1 μm withstands the bombardment from electrons during the lifetime of the machine operation. Two layers of coating are applied to the ceramic chamber for injection kickers: a 1μm-thick copper layer for by-passing the image charge, and a 0.1μm-thick titanium nitride (TiN) layer for a low secondary-electron yield, along with an exterior

Figure 30: Masking of the ferrite surface of the SNS ring extraction kicker for TiN coating. In order to avoid eddy-current heating, rise-time degradation, and high-voltage shorts, about 20% of the ferrite inner surface is uncoated.

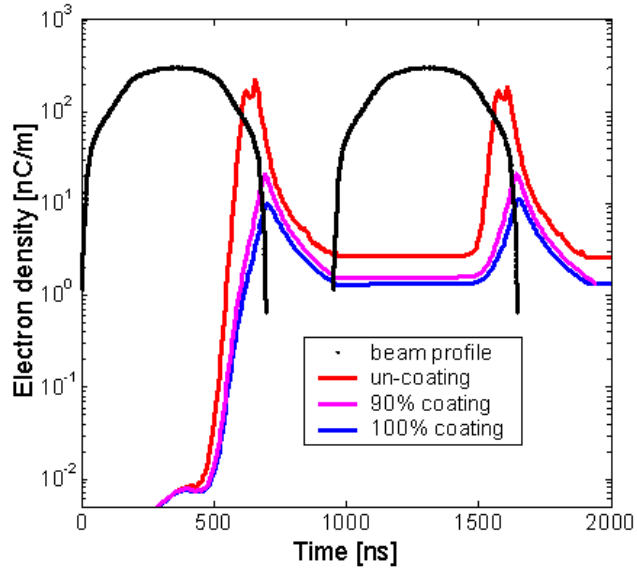

Figure 31: Computer simulation showing the reduction of electron-cloud density with a partial and a full TiN coating on the SNS extraction kicker.

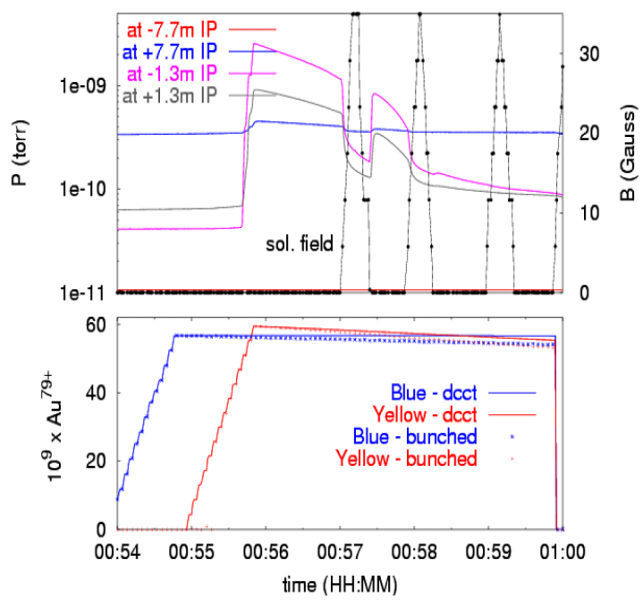

Figure 32: Reduction of vacuum pressure in the presence of the solenoidal field in a RHIC warm section [14].

metal enclosure for dc current by-pass. Such a design allows the passage of the image current above a frequency of the lowest betatron sideband (∼200 kHz) without degrading the magnetic-field penetration (a rise time of about 200μs), eddy-current heating, and beam-induced heating. For the ferrite of the extraction kicker inside the vacuum pipe, a special coating pattern is selected to avoid eddy-current heating, rise-time degradation, and high-voltage shorts, as shown in Fig. 30. Measurements of TiN-coated surfaces indicate a reduction of SEY by more than half of an unit (Fig. 3) [27]. Fig. 31 shows the expected reduction of the electron density with a partial and a full TiN coating. Vacant ports are available for additional pumping, if needed, to accommodate a higher level of outgassing from the rougher coated surface. The present magnet and vacuum chamber design does not allow NEG film coating which requires in-situ baking.

Beam scrubbing at an electron dose level of 1 mC/mm^2 can further condition the vacuum surface during operations [43]. For the SNS ring, vacant ports can house turbo pumps to function at a vacuum pressure above 10^{-6} Torr. Extended beam storage in the ring is planned to accelerate the scrubbing process.

5.2 Solenoids

Solenoidal magnetic field helps to confine the motion of electrons to be in parallel to the vacuum pipe surface, effectively reducing the electron multipacting. Fig. 32 shows the measured reduction of vacuum pressure in a RHIC warm section when the solenoidal fields are applied [14].

Solenoids are implemented on the vacant straights (about 5 m) of the collimation region of the SNS ring. The solenoid field B_ϕ of about 50 G is so strong that the radius $r_\phi = m_e v_e / eB_\phi$ (12 mm for 300 eV electrons) of electron motion is small compared with the pipe radius, as shown in Fig. 33. Effects on the proton beam can be minimized by alternating the polarities of the solenoids observing betatron-phase variations. Skew quadrupoles can further be used to correct the coupling.

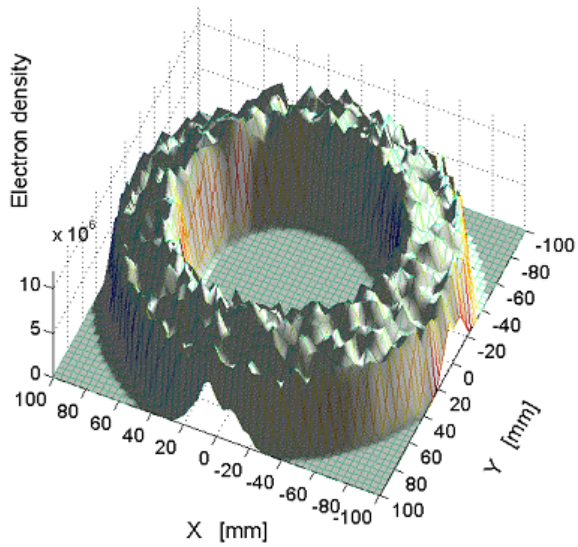

Figure 33: Computer simulation showing the confinement of electron cloud by the solenoidal field in the SNS ring.

5.3 *Clearing electrodes*

Clearing electrodes have long been used to mitigate electron-cloud effects in a coasting beam by locally changing the beam potential that traps the electrons [2, 3]. For a bunched beam, the electrodes can alter the multipacting pattern (frequency and energy gain) to effectively suppress the electron generation even if the applied voltage is much less than the beam potential, as shown in Fig. 34 [44].

For the SNS ring, a dedicated clearing electrode is implemented inside the stripping-foil assembly (Fig. 22). A voltage up to 10 kV can be applied, adequate to suppress multipacting in the injection region. BPMs around the ring are designed to be also used as clearing electrodes capable of providing a voltage up to ± 1 kV, adequate to locally reduce the multipacting frequency (Fig. 35).

5.4 *Others*

In order to reduce the electrons trapped by the residual beam in the beam gap of the SNS ring, a gap-clearing kicker is designed to clear the 250 ns gap during the last 100 of the 1060-turn accumulation [46]. By resonantly exciting coherent betatron oscillations, beam residuals are driven into the primary collimator, where beam loss is measured with a gated fast loss monitor. For the SNS ring, vacuum ports are screened, and steps in the vacuum pipe are tapered at 1-to-3 ratio to reduce peaked electric fields causing electron emission. A vacuum pressure of about 10^{-8} Torr ensures low electron generation from gas ionization. Possibilities of mitigating the e-p instability with wide-band resistive feedback are also under investigation [47].

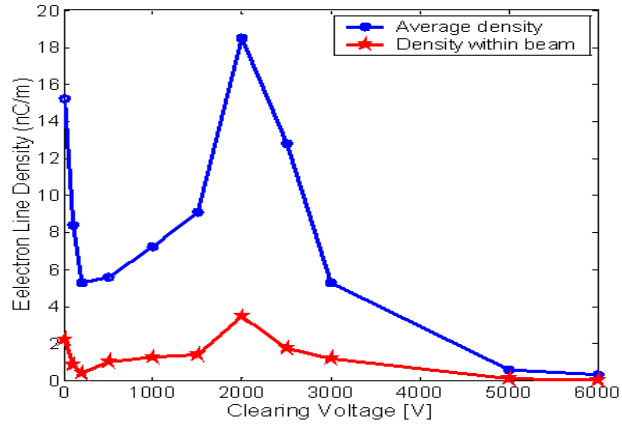

Figure 34: Simulation of the SNS ring showing the electron density as a function of the applied clearing electrode voltage. The peak beam potential is about 10 kV. The beam potential at the time of electron multipacting is about 2 kV. Such non-monotonic characteristics only applies to the long-bunch multipacting regime.

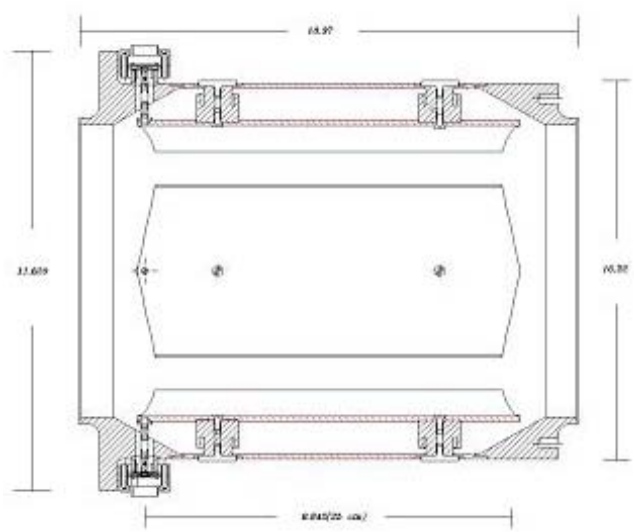

Figure 35: Floating-ground BPM for the SNS ring [45].

6 BEAM-DYNAMICS CHALLENGES

Electron-cloud effects limit the RHIC upgrade path toward higher intensity and luminosity, and the SNS potential beyond the design beam intensity and power. During the past four decades, many progresses have been made in the field of electron cloud. However, the understanding of the subject remains incomplete.

Among many open challenges are (1) understanding of surface science underlying secondary emission and gas desorption and guidance on surface treatment (2) dynamic model on vacuum pressure rise incorporating desorption, pumping, and ionization, and comparison with measurements; (3) instability theory and simulation that satisfactorily reproduces long-bunch regime data (PSR) and predicts

high-intensity ring performance (SNS, J-PARC); (4) self-consistent treatment of electron-cloud formation and beam instability in the simulation codes; (5) systematic benchmarking of simulation codes, and benchmarking with experimental data; (6) reliable diagnostics for both warm and cold regions; and (7) wide-band damping of fast, single-bunch electron-cloud instability.

We are indebted to our colleagues in the e-cloud community, and to colleagues on RHIC and SNS projects, especially A. Aleksandrov, G. Arduini, M. Bai, J. Brodowski, P. Cameron, N. Catalan-Lasheras, A. Chao, R. Connolly, S. Cousineau, V. Danilov, D. Davino, A. Fedotov, M. Furman, O. Gröbner, H. Hahn, P. He, S. Henderson, N. Hilleret, H. Huang, Y. Y. Lee, H. Ludewig, R. Macek, W. Meng, R. Michnoff, C. Montag, M. Pivi, M. Plum, C. Prior, V. Ptitsin, D. Raparia, G. Rees, N. Simos, F. Ruggiero, T. Satogata, H. Schonauer, N. Simos, S. Tepikian, P. Thieberger, R. Todd, J. Tuozzolo, F. Zimmermann, B. Zotter. We thank F. Zimmermann for the careful reading and corrections of the manuscript.

7 REFERENCES

[1] G.I. Budker, G.I. Dimov, V.G. Dudnikov, Proc. Intern. Sym. Electron and Positron Storage Rings, Saclay (1966, Orsay, Univ. de France) VIII-6-1

[2] H. Hereward, CERN Report 71-15 (1971)

[3] E. Keil, B. Zotter, CERN Report CERN-ISR-TH-71-58 (1971)

[4] A. Gröbner, Proc. 1977 Int. Conf. on High Energy Accelerators, Protvino (1977) p. 277.

[5] D. Neuffer, et al, Nucl. Instru. Meth., **A321** (1992) 1

[6] J. Wei, Reviews of Modern Physics, **75** (2003) 1383

[7] R. Macek, A. Browman, D. Fitzgerald, et al, Proc. Part. Accel. Conf., edited by P. Lucas, S. Webber (IEEE, Chicago, 2001), p. 688

[8] F. Zimmermann, Proc. Part. Accel. Conf., edited by P. Lucas, S. Webber (IEEE, Chicago), p. 666

[9] M. Izawa, Y. Sato, T. Toyomasu, Phys. Rev. Lett., **74**, (1995) 5044

[10] K. Ohmi, Phys. Rev. Lett., **75** (1995) 1526

[11] Z.Y. Guo, et al, Proc. 1st Asian Part. Accel. Conf., Tsukuba, Japan (1998)

[12] S.Y. Zhang, BNL Tech. note C-A/AP/67 (2001); Euro. Part. Accel. Confe. (2004) 944

[13] W. Fischer, M. Blaskiewicz, J.M. Brennan, T. Satogata, Phys. Rev. ST-AB, **5** (2002) 124401

[14] U. Iriso, et al, BNL Tech. note C-A/AP/129 (2003); ICFA Beam Dynamics Newsletter, **33** (2004) 128; BNL Tech. note C-A/AP/191 (2005)

[15] See, for example, articles in the ICFA Beam Dynamics Newsletter, **33**, edited by K. Ohmi and M. Furman (2004)

[16] J. Wei, D.T. Abell, J. Beebe-Wang, et al, Phys. Rev. ST-AB, **3** (2000) 080101; J. Wei, M. Blaskiewicz, J. Brodowski, et al, Part. Accel. Confe. Portland (2003) 2598

[17] F. Zimmermann, LHC Project-Report 95, and SLAC-PUB-7425 (1997).

[18] M.A. Furman, KEK Proc. 97-17, edited by Y. H. Chin (1997) p. 170.

[19] F. Ruggiero, G. Rumolo, F. Zimmermann, Phys. Rev. ST-AB, **2** (2001) 012801; Erratum **2** (2001) 029901.

[20] V. Danilov, A. Aleksandrov, J.D. Galambos, et al, AIP Conf. Proc. 496, edited by T. Roser and S.Y. Zhang (AIP, New York 1999), p. 315.

[21] L. Wang, et al, Phys. Rev. ST-AB, **5** (2002) 124402

[22] J. Wei, R. Macek, CERN Report CERN-2002-001 (2002)

[23] L. Wang, A. Chao, H. Fukuma, ECLOUD 2004 (Napa, 2004)

[24] R. Cimino, I.R. Collins, M.A. Furman, et al, Phys. Rev. Lett., **93** 014801 (2004)

[25] L. Wang, M. Blaskiewicz, J. Wei, W.T. Weng, K. Ohmi, R. Macek, Phys. Rev. **E70** (2004) 036501

[26] M. Pivi, et al, CERN Report CERN-2002-001 (2002)

[27] P. He, H. Hseuh, M. Mapes, et al, submitted to J. Vacuum Science Technology (2003)

[28] A. Gröbner, these proceedings

[29] H. Hseuh, et al, ECLOUD 2004 (Napa, 2004); private communications (2005)

[30] J. Wei, *Longitudinal Dynamics of the Non-Adiabatic Regime in the Alternating-Gradient Synchrotrons*, Ph.D. dissertation (1989, revised 1994, Stony Brook)

[31] M. Blaskiewicz, Part. Accel. Confe. (2003)

[32] C. Montag, J. Kewisch, D. Trbojevic, F. Schmidt, Phys. Rev. ST-AB, **5** (2002) 084401

[33] Beam experiments participated by J. Wei, U. Iriso, M. Bai, M. Blaskiewicz, P. Cameron, R. Connolly, W. Fischer, H. Huang, R. Lee, R. Michnoff, V. Ptitsin, T. Roser, T. Satogata, S. Tepikian, L. Wang, S.Y. Zhang, to be published (2005)

[34] S.Y. Zhang, BNL Tech. note C-A/AP/107 (2003)

[35] R. Connolly, P. Cameron, T. Shea, etal, BNL Technical note SNS/59 (1999)

[36] M. Plum, Part. Accel. Conf. (1995) 3403

[37] Y.Y. Lee, et al, Part. Accel. Conf. (2005), to be published

[38] L. Wang, et al, Part. Accel. Conf. (2005), to be published

[39] P. Thieberger, A.L. Hanson, D.B. Steski, et al, Phys. Rev., **A 61** (1999) 042901.

[40] N. Catalan-Lasheras, Y.Y. Lee, H. Ludewig, et al, Phys. Rev. ST-AB, **4** (2001) 010101.

[41] D. Raparia, private communications (2005)

[42] H. Huang, private communications (2005)

[43] S.Y. Zhang, et al, Part. Accel. Confe. (2003) 3419

[44] L.F. Wang, D. Raparia, J. Wei, et al, Phys. Rev. ST-AB, **7** (2004) 034401

[45] P. Cameron, et al, private communications (2003)

[46] R. Witkover et al, PAC99 p. 2250; N. Catalan-Lasheras et al PRST-AB **4** (2001) 010101

[47] S. Henderson, private communications (2004)